Nonlocal Temporal Interferometry for Highly Resilient Free-Space Quantum Communication

Lukas Bulla[1,2,*] Matej Pivoluska[1,2,3,4,†] Kristian Hjorth,[1,5] Oskar Kohout,[1,6,7] Jan Lang,[1] Sebastian Ecker,[1,2]
Sebastian P. Neumann[1,2] Julius Bittermann[1,2] Robert Kindler[1,2] Marcus Huber[1,8,‡]
Martin Bohmann[1,2,§] and Rupert Ursin[1,2,∥]

[1]*Institute for Quantum Optics and Quantum Information (IQOQI), Austrian Academy of Sciences,
Boltzmanngasse 3, 1090 Vienna, Austria*
[2]*Vienna Center for Quantum Science and Technology (VCQ), Faculty of Physics, University of Vienna,
Boltzmanngasse 5, 1090 Vienna, Austria*
[3]*Institute of Computer Science, Masaryk University, 602 00 Brno, Czech Republic*
[4]*Institute of Physics, Slovak Academy of Sciences, 845 11 Bratislava, Slovakia*
[5]*Department of Physics, Faculty of Natural Sciences,
Norwegian University of Science and Technology (NTNU), NO-7491 Trondheim, Norway*
[6]*Fraunhofer Institute for Applied Optics and Precision Engineering IOF,
Albert-Einstein-Strasse 7, 07745 Jena, Germany*
[7]*Friedrich-Schiller-Universitt Jena FSU, Frstengraben 1, 07743 Jena, Germany*
[8]*Vienna Center for Quantum Science and Technology (VCQ), Atominstitut,
Technische Universität Wien, Stadionallee 2, 1020 Vienna, Austria*

Entanglement distribution via photons over long distances enables many applications, including quantum key distribution, which provides unprecedented privacy. The inevitable degradation of entanglement through noise accumulated over long distances remains one of the key challenges in this area. Exploiting the potential of higher-dimensional entangled photons promises to address this challenge, but poses extreme demands on the experimental implementation. Here, we present a long-range free-space quantum link, distributing entanglement over 10.2 km with flexible dimensionality of encoding by deploying a phase-stable nonlocal Franson interferometer. With this distribution of multidimensional energy-time entangled photons, we analyze the achievable key rate in a dimensionally adaptive quantum key distribution protocol that can be optimized with respect to any environmental noise conditions. Our approach enables and emphasizes the power of high-dimensional entanglement for quantum communication, yielding a positive asymptotic key rate well into the dawn of the day.

Subject Areas: Optics, Quantum Physics,
Quantum Information

I. INTRODUCTION

Securing communication against eavesdropping is one of the most important challenges of modern society with its constantly increasing use in information technology. The security of our current encryption methods, however, is challenged by the computational power of emerging

*lukas.bulla@oeaw.ac.at
†mpivoluska@mail.muni.cz
‡marcus.huber@tuwien.ac.at
§martin.bohmann@oeaw.ac.at
∥rupert.ursin@oeaw.ac.at

quantum computers and vulnerable to device hacking. A solution to these threats can also be found in the quantum realm, namely by means of quantum key distribution (QKD) [1,2]. In contrast to classical cryptography relying on computational hardness assumptions, the security of QKD is based on the very nature of physical laws. In particular, quantum entanglement [3] allows us to establish a secure cryptographic key between two communicating parties, which can be used to establish a secure communication channel. Security of a cryptographic key produced by an entanglement-based QKD protocol is assured by the monogamy of quantum entanglement. This concept can be extended to multiuser communication networks [4–7] and thus has a great potential to revolutionize the way secrecy of communication is protected. Over the past decade, laboratory proof-of-principle experiments were turned into real-world entanglement-based QKD implementations over deployed fiber [8,9], horizontal free space [10–14],

and satellite-Earth links [15–19]. Nevertheless, there are fundamental challenges to overcome in free-space QKD communication channels. Among these are long communication distances that cause high signal loss. With increasing loss a point appears where intrinsic dark counts and the presence of high intrinsic background count rates, which generally make QKD during the day considerably more difficult, become dominant. To overcome these limitations it is possible to exploit fundamental quantum correlations even further by leveraging properties of high-dimensional quantum states. This can be achieved through hyperentanglement using simultaneous entanglement in different degrees of freedom (d.o.f.) [20,21] and using d.o.f. that intrinsically offer high-dimensional entanglement such as the time-energy d.o.f. [22–24]. Indeed, such high-dimensional quantum states do not only offer an increased quantum communication capacity [25–28], but also provide improved noise robustness in entanglement distribution [29,30]. These remarkable features can be exploited in a QKD protocol with high-dimensional encoding [31]. Although these features have been analyzed in theory using simplified noise models and later also demonstrated under laboratory conditions [32], a fully fledged demonstration of the benefits of high-dimensional quantum states over a real-world quantum channel has been missing until today.

In this paper, we implement the first high-dimensional entanglement-based real-world free-space link and demonstrate its practical usefulness by computing the asymptotic key rate in the subspace encoding QKD protocol [31]. A significant innovation of this approach is that it enables an adaptive and flexible encoding, allowing for an optimized QKD performance even under very harsh environmental conditions. By establishing a 10.2-km-long free-space quantum communication channel over Vienna's metropolitan area, we expose the quantum channel to the major challenges of free-space quantum communication and show that our schemes help under all circumstances where noise plays, or starts to play, a dominant role. To this end, we develop and advance techniques that will enable fundamental and applied experiments based on phase-stable nonlocal interference over free space and long distances. Our approach provides a pathway that harnesses the advantages of high-dimensional quantum correlations to overcome the major challenges of real-world quantum communication, paving the way for a resilient and resource-efficient quantum internet.

II. RESULTS

A. Experiment and implementation

To exploit the high-dimensional nature of the time-energy d.o.f., we produce entangled photon pairs and measure two-photon interference in a Franson-type nonlocal interferometer [33] over a long-range free-space link. The long-range experiment is carried out between the sending party at IQOQI Vienna (Alice) and the receiving

party (Bob), located at a 10.2 km free-space distance at Bisamberg in Lower Austria (see Fig. 1).

The free-space quantum channel runs north-northeast (bearing 10.89°), mainly across Vienna's metropolitan area and over the Danube river to Bisamberg. The strong influence of atmospheric turbulence on the signal propagating over such an urban environment leads to fluctuation in the angle of arrival of 150 μrad and an average channel loss of $\sim$25 dB, comparable to low Earth orbit satellite links [34].

We use spontaneous parametric down-conversion (SPDC) to create hyperentangled photon pairs at Alice's laboratory. The entangled-photon-pair source is operated in a Sagnac configuration [35,36] bidirectionally pumped by a 404.53 nm continuous-wave laser producing photon pairs at 809 nm, with a coherence time of $\tau_p \sim 3$ ps defined by the periodically poled potassium titanyl phosphate (ppKTP) crystal length (see Appendix A 1). The resulting quantum state features both time-energy and polarization entanglement and can be approximated by

$$|\Psi\rangle_{AB} = \int dt f(t)|t,t\rangle \otimes (|H,H\rangle + e^{-i\phi}|V,V\rangle), \quad (1)$$

where $f(t)$ is a continuous function of time, determined by the coherence time of the laser, and H (V) indicates the horizontal (vertical) polarization state. One photon of a pair is detected locally at Alice's laboratory while the other is transmitted over the turbulent free-space link to Bob. The transmitter is composed of a 75 mm achromatic sending lens and the beacon receiving 350 mm Newtonian telescope mounted on top of a hexapod. Bob's receiver consists of a Cassegrain telescope with a 254 mm aperture also mounted on a hexapod in addition to the entire receiving module. To achieve consistent long-time-averaged count rates over the free-space link, we implement a bidirectional angular tracking of 532 nm beacon lasers at the transmitter and the receiver [10].

Each communicating party is equipped with a receiving module capable of performing measurements in two incompatible bases: the time-of-arrival basis (TOA) and the time-superposition (TSUP) basis (see Fig. 1). To measure in the TSUP basis, the first-ever reported nonlocal Franson-type interferometer [33] separated by a distance of 10.2 km free-space was build. In the TOA basis, we detect the arrival time of the photons as well as their polarization (HV measurement), effectively decreasing the accidental noise photons as compared to a polarization insensitive bucket detector.

To perform the TSUP-basis measurements, we implement unbalanced Mach-Zehnder interferometers (MZI) with a path difference of $\tau_{MZI} = 2.7$ ns, which exceeds the coherence length of the SPDC photons ($\tau_p \ll \tau_{MZI}$).

By using polarizing beam splitters (PBS) in the MZIs, we measure postselection-free Franson interference by mapping the polarization entanglement to the interferometer
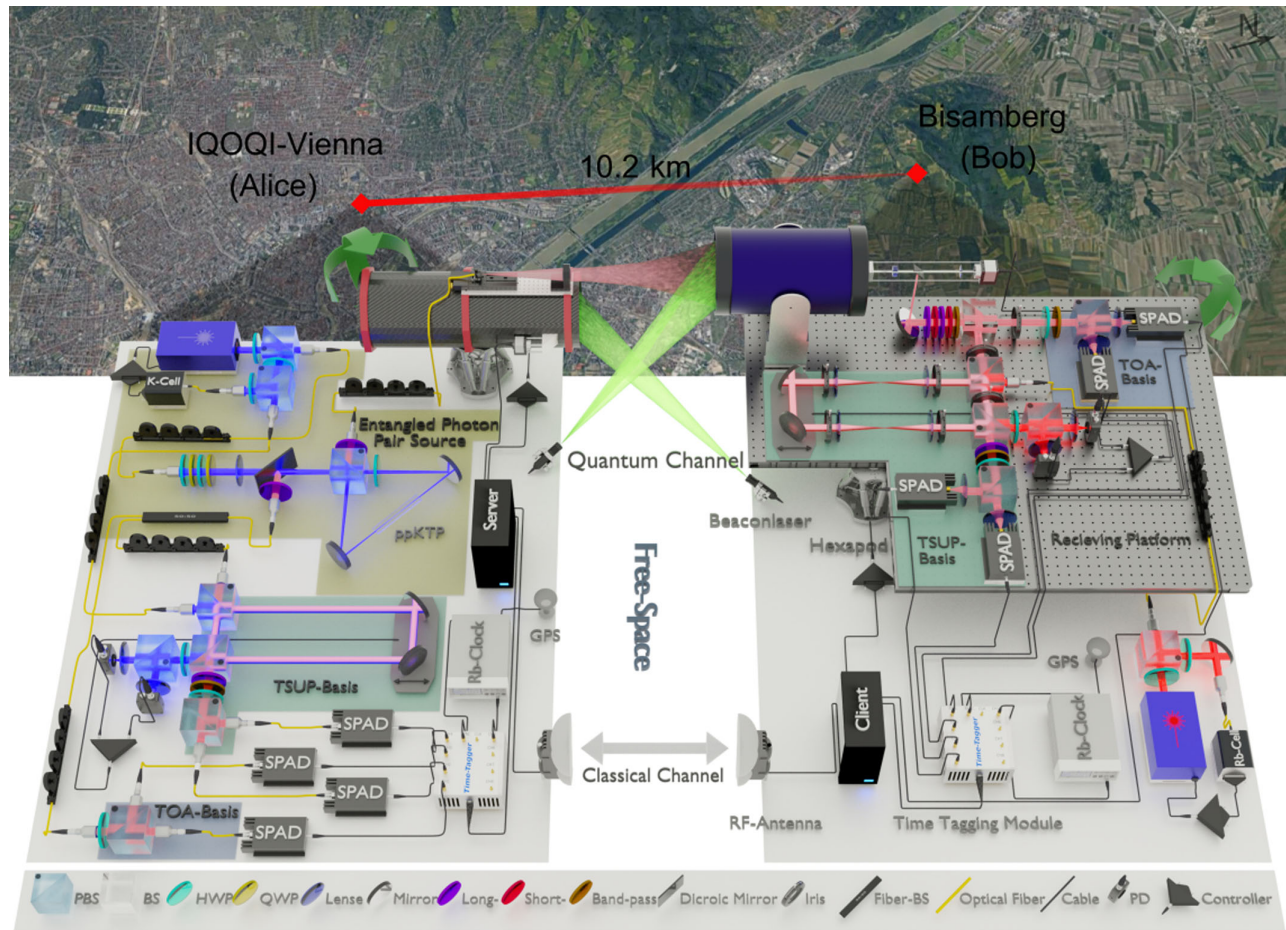
FIG. 1. Illustration of the high-dimensional quantum key distribution experiment. The free-space link is established between the sender at IQOQI Vienna (Alice) and the receiver at Bisamberg (Bob) in Lower Austria over a distance of 10.2 km. The hyperentangled photon source is pumped by a ^{39}K stabilized laser at 404.532 nm. The hyperentangled state is set by adjusting a combination of half-wave (HWP) and quarter-wave (QWP) plates. The hyperentangled photons produced at 808.9 nm by a ppKTP crystal are separated and guided to the receivers Alice and Bob who by the aid of a 50:50 beam splitter (BS) randomly measure their photons in the time-of-arrival (TOA) and the temporal superposition (TSUP) basis. By using polarizing beam splitters (PBS) in the Mach-Zehnder-Interferometers (MZI) followed by a polarization measurement in the D/A basis, we achieve postselection-free Franson interference. While Alice analyzes her photons locally, Bob's photons are transmitted over the free-space link to Bisamberg. The MZI is locked to the pump laser stabilized by a piezoactuator controlled by the interferometric intensity changes measured by two photodetectors (PD). The photon detection events are recorded by single-photon avalanche diodes (SPAD), time stamped by the time-tagging module, and streamed to the server. The photons received at Bob are guided to his detection modules where we use several irises as optical baffles and combinations of optical filters to reduce the influence of background radiation. Bob's measurements are corresponding to Alice's, with the difference of having two $4f$ systems in the MZI to compensate for the atmospheric turbulence; Bob's MZI is locked to a ^{87}Rb stabilized laser at 780.23 nm.

paths followed by a polarization measurement in the D/A basis, effectively erasing the which-path information [14]. Thus, we exploit the hyperentanglement of the photon pairs to improve the time-energy TSUP measurement by means of polarization entanglement (see Appendix A 2).

To enable nonlocal interference over a long-distance free-space link, which has to be phase stable over significant times, we devise and implement several experimental features. To counteract the detrimental effect of atmospheric turbulence and reduce mode mismatch between long and short interferometer paths, caused by the difference in angles of arrival, we place two $4f$ systems in the long path of Bob's MZI [5,37].

To reach the required high subwavelength demands in terms of phase stability and to avoid phase drifts due to thermal expansion of the MZIs, we stabilize them at the sender and the receiver by using two lasers locked to atomic hyperfine structure transitions [38], achieving frequency fluctuations below 1 MHz. By using the pump laser as stabilization laser we additionally lock the phase ϕ of the state Eq. (1) to the phase of both interferometers (see Fig. 1).

An essential point for using the time-energy d.o.f. over long distances is to keep the reference time frames of Alice and Bob synchronized, which is demanding due to relative drifts of the clocks and the small temporal size of time bins. In order to solve this problem, we use Global-Positioning-System-synchronized Rb clocks on both sides to lock the time-tagging modules for long-term stability. The time-tagging modules provide time stamps for each of the eight photon-detection events and stream the data to the client and server data storage, respectively. Furthermore, it is necessary to compensate for relative short-term clock drifts $T_{dev} \sim 30$ ps/s by tracking via the statistical photon intensity correlation function to gain accuracy [39,40].

B. High-dimensional state encoding from discretization

Because of the finite precision of recording each individual photon's time of arrival, we implement discretized measurements in the energy-time d.o.f. These discretized measurements work with notions of *time frames* and *time bins* [29,31]. A time frame defines a time interval in which the arrival of up to one photon is expected and its length is one of the free parameters we can choose to manipulate the effective state dimension. The time frame is further subdivided into time bins which determine whether Alice's and Bob's recorded photon arrival times are correlated. One can then specify a time frame of length Δt_f that starts at time t_0 and consists of d time bins of length Δt_b. The measurement outcome in the TOA basis, labeled $j \in \{0, ..., d-1\}$, indicates the time of arrival in a time bin starting at time $t_0 + j\Delta t_b$. We use the time of arrival as the standard basis and identify each time bin to a basis vector. Therefore, an outcome j corresponds to the projection onto a state $|j\rangle$. The TSUP-basis measurement, on the other hand, performs a projection onto the superposition $(1/\sqrt{2})(|j\rangle \pm |j+k\rangle)$, which comes from the indistinguishability between the propagation of entangled photons through the short and the long arms of the MZI. Notably, we require that $k = \tau_{MZI}/\Delta t_b$ to be an integer. This ensures that starting times of both $|j\rangle$ and $|j+k\rangle$ are exactly τ_{MZI} apart and the interference can be observed. The above-mentioned discretization effectively reduces the continuous quantum state introduced in Eq. (1) to its discretized form:

$$|\Psi\rangle_{AB} = \sum_{j=0}^{d-1} \frac{1}{\sqrt{d}}|j,j\rangle \otimes \frac{1}{\sqrt{2}}(|H,H\rangle + e^{-i\phi}|V,V\rangle). \quad (2)$$

Overall, our measurement setup allows us to measure elements of discretized states of the form in Eq. (2), giving access to $(d \times d)$-dimensional entangled states. In particular, we can choose to address different discretizations by choosing different values of Δt_f and Δt_b, which represent different levels of fine graining. This fine-graining process bears the great advantage that it can be adapted and optimized to the various channel and measurement

conditions in postprocessing. In the following, we demonstrate this outstanding feature in an experiment and show that it can be used for optimizing entanglement transfer and secure key rates for a wide range of channel noise contributions under real-world conditions. In particular, we are working with a time-frame length of twice the MZI imbalance (5.4 ns), which we divide into multiple time bins to operate on Hilbert-space sizes varying between 4×4 and 36×36. Where the choice of 5.4 ns frame length leads to well-defined TSUP measurements (see Appendix A 4). Furthermore, we do not certify entanglement for $d < 4$ over the free-space link due to the intrinsic low signal-to-noise ratio [29], and $d = 36$, corresponding to $\Delta t_b = 150$ ps, is the highest dimension achievable beyond which the signal is degraded due to limitations in the timing synchronization and detector jitter (see Appendix A 7).

C. High-dimensional entanglement distribution

We first demonstrate that we indeed distribute entanglement in the time-energy d.o.f. of the noisy free-space channel. For this purpose, we exploit a tight and straightforward entanglement witness $\hat{\mathcal{W}}_d$ that acts on qubit subspaces of the distributed d-dimensional state. Entanglement is certified when the expectation values $\langle \hat{\mathcal{W}}_d \rangle$ exceed the value of 1.5 (see Ref. [41] and Appendix A 5).

We experience different types of noise during the 4 h measurement run with distinct influences on entanglement distribution and the corresponding optimal state dimensionality. The strongest source of noise in the long term is the continuously increasing background radiation from the Sun which finally exceeds the level of noise tolerable to observe an entanglement witness at 06:46 (see Fig. 2). Notably, this is more than 1.5 h after sunrise with a noise-count rate on Bob's side that is 20 times larger than the signal from the source. Other noise types are minor instabilities in the interferometers, caused by vibrations or strong airflow, leading to dephasing noise in the TSUP basis and the dark count rate of the detectors both constantly adding to the noise count. Hence, our results show that time-energy entanglement can be successfully distributed in the presence of these different noise contributions over a real-world quantum channel.

D. Noise-resistant time-energy quantum key distribution

Here we demonstrate that it is possible to harness the distributed entanglement for secure quantum communication. For this purpose, we employ a recently introduced high-dimensional subspace QKD protocol [31] for which we estimate the achievable asymptotic key rates and demonstrate the advantage of high-dimensional states for quantum communication over urban noisy free-space channels.

The calculated asymptotic key rates, optimized with respect to dimension d, are shown in Fig. 3. We clearly observe that the optimal dimensionality changes with the
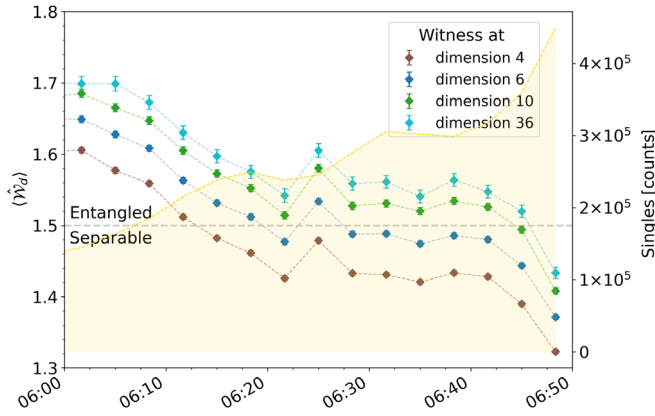
FIG. 2.   Entanglement witness. Expectation values of entanglement witness $\hat{\mathcal{W}}_d$ of the discretized distributed state are plotted for different discretization dimensions $d = \{4, 6, 18, 36\}$. Values above 1.5 certify entanglement [41]. The witness is evaluated for data obtained by integrating over 200 s blocks of time-tagged detector event streams, which corresponds to typical passage times of satellites [42]. To show the increasing noise from sunlight the received single-photon count rates at Bob's side are plotted in the background. From the plot it is apparent that with sunrise the channel conditions start to deteriorate rapidly. Nevertheless, entanglement can be certified well up to 1.5 h after the sunrise (05:03). Further, discretizations with higher dimensionality outperform the lower-dimensional ones in all cases.

noise conditions in the channel over time. For low noise levels, lower dimensions generate the highest key rates, while higher dimensions show the possibility to obtain a secure key even under the influence of strong noise,

particularly during daylight. This enables us to adaptively choose the best state dimension, featuring a flexible and versatile approach for QKD under varying noise conditions. The optimal dimension strongly depends on the type of noise level the signal is experiencing. During precipitation, we observe that the optimal dimension increases (see Fig. 3 around 03:45). Also during dawn, the ever rising level of background radiation requires an increase of the dimension d to acquire the optimal key (see Fig. 3 between 04:30 and 05:35).

III. DISCUSSION

We demonstrate the distribution of high-dimensional entangled photon pairs over a 10.2-km-long free-space link under various detrimental noise conditions. This is achieved by advancing both experimental techniques and theoretical tools, tailored for the optimal exploitation of the high-dimensional quantum state. These results are the first proof-of-principle demonstration of energy-time entanglement-based QKD over a long-distance free-space channel. The link runs partly over the urban inner-city area which is heavily populated and causes very strong turbulences. The developed quantum-state discretization and encoding toolbox (see Appendix A 4) enables the optimization of QKD under various noise conditions, providing an adaptive and versatile avenue toward noise-resistant quantum communication for the future quantum internet.

The heart of our contribution consists of an innovative way in which we measure and exploit high-dimensional energy-time entanglement. This requires the first realization of a
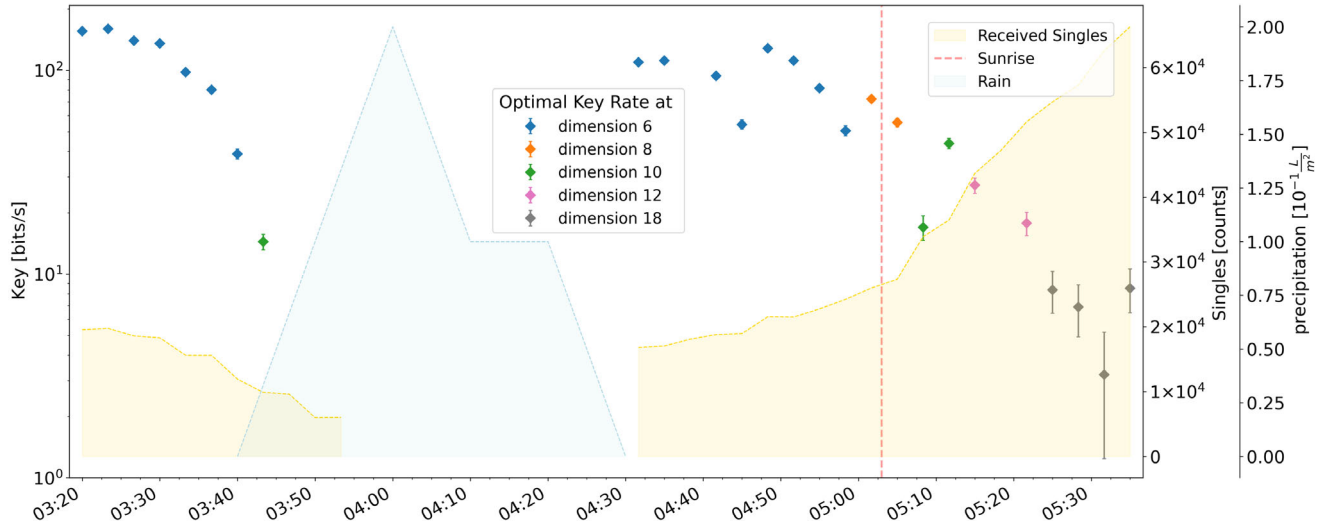

FIG. 3.   Achievable key rate. The achievable key rates are plotted over the measurement time of the experiment. The key rate is evaluated for data obtained by integrating over 200 s blocks of time-tagged detector event streams. For each interval the optimal nonzero key-rate value is plotted, using different colors to indicate the corresponding best dimensionality. The orange line indicates sunrise, and we show the rain data and single photon counts as a measure for background radiation. From the plot it can be clearly seen that our noisy free-space channel can be used to distribute a cryptographic key under various noise conditions, even for considerable time after the break of the day. Overall, the dimension of the discretization which achieves the largest key rate increases with the increasing background radiation, thus demonstrating superior noise resistance of high-dimensional encoding.

Franson-type interferometer used over a long-distance free-space link. It is implemented by the deployment of two interferometers and one photon-pair source, all being phase locked in reference to each other separated by a 10.2 km free-space link. Furthermore, we implement two $4f$ lens systems in the receiver's interferometer to counteract the influence of wave-front distortion that otherwise would inhibit the interferometric measurement. For enabling a common reference frame in the time-energy d.o.f. between the communication parties, we had to implement a precise two-step clock synchronization approach which reached a precision of ~ 20 ps. These advances break ground for further work in quantum science over long distances and under harsh conditions ranging from fundamental tests, such as the study of Bell nonlocality, to advanced applications in quantum information.

Even though the implemented nonlocal interference measurements only allow for measurements in two-dimensional subspaces, our results provide optimal exploitation of the high-dimensional state space and its applications and benefits. We develop an entanglement-based QKD scheme that effectively utilizes the high-dimensional state space. It can be optimized and adapted concerning the communication channel imperfections, such as strong losses even during rainfall and high solar background radiation (see Fig. 3). This can be achieved by calculating the state-dimension trade-off between noise resistance and information capacity (see Appendix A 6). Furthermore, all adaptations can be applied in the postprocessing without any change in the setup or knowledge of the noise contribution prior to the measurement. This adaptability is what sets our time-bin implementation apart from high-dimensional QKD implementations using other d.o.f., where the total dimensionality typically needs to be set before the start of the experiment. Importantly, we also demonstrate that it is necessary to use a state dimension of at least four in our experiment to obtain a positive key rate and that the optimal dimension is often found for even larger total dimensionality, i.e., genuinely requires the usage of more than simple qubit discretizations.

We show that both entanglement and secure key rates can withstand different noise contributions within the highly turbulent atmospheric channel long after sunrise (see Figs. 2 and 3). The implemented channel is comparable with low Earth orbit satellite links regarding losses and turbulence [43,44], thus demonstrating its relevance for global quantum communication. Although challenging, it is possible to implement the source and detection modules with the required stabilization and synchronization on spaceborne platforms [16].

Entanglement even persists further into the day and is still certifiable without any further assumptions, when no key can be produced any more. On the one hand, this could prove useful for other quantum communication scenarios in which entanglement is always known to provide an advantage, such as entanglement-assisted classical communication [45]. On the other hand, this should motivate further research into more elaborate quantum key distribution protocols. Since distillable entanglement [46] can still be shown, one would assume that it should be possible to distill a useful key from the noisy quantum states. Current protocols, however, sacrifice too much key to perform error correction preventing them from providing a positive key rate.

Altogether, our results pave the way for an extensive field of fundamental and applied research in quantum science and technology that explores and exploits the potential of high-dimensional quantum states.

APPENDIX

1. Hyperentangled photon-pair source

The source is built in a Sagnac configuration deploying a 30-mm-long type-II ppKTP crystal which is bidirectionally pumped without any active phase stabilization. By superposing the clockwise and counterclockwise SPDC photons, a polarization-entangled two-photon state is created. Further, due to the energy conservation of the SPDC process, energy-time entanglement emerges within the laser's coherence length, which leads to the hyperentangled state in Eq. (1). A laser stabilized to a potassium (^{39}K) hyperfine transition pumps the source at $\lambda = 404.453$ nm with a power of $P = 28.5$ mW and a long-term stability of ≤ 1.8 fm/h. The signal and idler photons are produced in a degenerate spectral mode at $\lambda = 808.9$ nm. To evaluate the source performance without link, we carry out local

measurements yielding a pair rate of $R_{cc} \sim 65$ kcps/mW with a local heralding efficiency of $\eta \sim 26\%$, including detector efficiency and source imperfections. Additionally, we measure a local visibility of the entangled state in the horizontal/vertical (diagonal/antidiagonal) polarization basis of $V_{HV} \sim 99\%$ ($V_{DA} \sim 98\%$).

2. Detection modules

The detection modules consist of two submodules, namely the superposition (TSUP) and the time-of-arrival modules, corresponding to the respective measurement basis. Both modules receive the incoming beam via a beam splitter to ensure random basis choice. Before detection, the TOA basis is further multiplexed in the polarization d.o.f. by means of a polarizing beam splitter. For the TSUP measurement we deploy unbalanced MZIs consisting of two polarizing beam splitters and a path difference between the long and short arm of $\Delta L \sim 80.8$ cm, which corresponds to a propagation-time difference of $\tau_{\mathrm{MZI}} \sim 2.7$ ns. The polarizing beam splitters are used to map the polarization-entangled state to the time-energy entangled state. This means that polarization states are mapped to temporal modes as $|V\rangle_{\mathrm{pol}} \rightarrow |L\rangle_{\mathrm{path}}$ and $|H\rangle_{\mathrm{pol}} \rightarrow |S\rangle_{\mathrm{path}}$, where $|S\rangle_{\mathrm{path}}$ and $|L\rangle_{\mathrm{path}}$ represent the short and long paths of the interferometers, respectively. The measurement after the interferometers is performed in the D/A basis to delete the photon's which-path information. This method facilitates a postselection-free Franson interferometer which increases the efficiency of the energy-time analyzers by a factor of 2. Each MZI is locked to a stabilized laser via a piezoactuator in a closed control loop. For this purpose, we apply Doppler-free saturation-absorption spectroscopy to lock the lasers [47]. For Bob, we use a 780.23 nm laser with a ^{87}Rb cell; for Alice, we use the SPDC pump laser at 404.53 nm with a ^{39}K cell. The stabilization compensates for thermal drifts to keep the phase of the Franson interferometer stable within 1 MHz of relative phase error. Because of atmospheric wave-front distortion of the incoming beam, Bob's receiving interferometer has two $4f$ systems implemented in its long arm. These $4f$ systems map each incident angle of the arriving beam from the first to the second PBS. The $4f$ system has been used in the past as spatial filter and for spatial map [5,37,48]. This spatial mapping makes Franson interference possible despite the distorted wave front. The single-photon avalanche diodes (SPADs) are free-space detectors with a detection area of 150 μm in diameter on Bob's side and multimode-fiber-coupled SPADs on Alice's side. Locally, each Mach-Zehnder interferometer reaches an interference visibility of 95%.

3. Link establishment

The sending lens ($f = 274, 5$ mm) is a custom-made achromatic duplet designed at $\lambda = 780$ nm with a calculated spot size of $d \sim 50$ mm (Gaussian beam) at 10.2 km distance. It is mounted on top of a Newtonian telescope

($f = 1140$ mm) with an aperture of 350 mm, which is additionally used for pointing and tracking. Furthermore, a beacon laser ($\lambda = 532$ nm) is mounted on the telescope. On the receiving side, we choose an off-the-shelf Cassegrain telescope ($f = 2032$ mm) with an aperture of 254 mm. This choice is a result of a trade-off between availability, cost, loss, and weight. The telescope introduces a 6 dB geometric loss to the link budget due to the size and the central obstruction. Also, the receiver has a beacon laser mounted for bidirectional tracking. To avoid angular beam transfer from the receiving telescope to the setup and to optimize the pointing, the sending telescope and the entire receiver setup are mounted on hexapods. This link configuration enables bidirectional closed-control-loop tracking with 1 Hz on the beacon lasers with a 5 μrad resolution. We use a 532 nm pointing laser to easily separate the pointing signal from the quantum signal at 810 nm. Without tracking, with the best experienced environmental conditions the signal at 810 nm is steadily decreasing within 1 h to background noise levels. Additionally, without tracking, it would not have been possible to align the setup with respect to the link. During the alignment without tracking the signal is immediately lost due to the weight shifts and the mechanical stress to the optical setup. This method prevents beam wandering and keeps the signal intensity at the optimum. To reduce stray light on the receiver, multiple irises are placed in the setup and attached behind the telescope. A combination of long-pass, short-pass, and interference bandpass filters is placed in the incoming beam to minimize environmental noise further. The filters are chosen to lower noise in the overall sensitivity spectrum of Si-based detectors by 60 dB. With the exception of the bandpass filter with a bandwidth (FWHM) <1 nm at $\lambda = 808.9$ nm to ensure the narrow spectral filtering of the signal wavelength.

4. Discretization techniques

As we briefly describe in Sec. II, the crucial component of the discretization is the division of time-tagged detection event streams into time bins of length Δt_b. Subsequently, d subsequent time bins are collected into a time frame. As the quantum state of the photon pairs corresponds to a coherent superposition of arrival times, the information of the arrival time of a photon in one of the d time bins of a single time frame forms the computational basis of a d-dimensional Hilbert space. Counting from zero, the arrival in the jth time bin of the time frame is represented by a basis vector $|j\rangle$. Using the continuous entangled-state description presented in Eq. (1), the energy-time part of the (unnormalized) discretized state can be written as

$$|\Psi\rangle_{AB} = \sum_{j=0}^{d-1} c_j |j\rangle_A |j\rangle_B, \qquad (A1)$$

where $|c_j| = \int_{t_j}^{t_j + \Delta t_b} dt f(t)$, $f(t)$ is a continuous function of time, determined by the coherence time of the laser, and t_j denotes the starting time of the jth time bin. Note that if the coherence time of the laser is much longer than the length of a time frame $\Delta t_f = |t_{d-1} - t_0 + \Delta t_b|$, then $f(t) \approx \bar{f} = \text{const}$ in this interval, which leads to $c_j = \bar{f} \Delta t_b$ and, after normalization, to $|c_j| = 1/\sqrt{d} \; \forall \; j$.

In light of the discrete state description above, the TOA measurement can be trivially described as a projection onto the basis $\{|j\rangle\}_{j=0}^{d-1}$. The basic data unit associated with the corresponding joint measurement is a $d \times d$ correlation matrix $M_{\text{TOA}} = (m_{i,j})_{(i,j)}$, which in position $m_{i,j}$ contains the number of coincidences obtained in time bins $|i\rangle$ and $|j\rangle$ on Alice's and Bob's side, respectively, meaning $m_{i,j} \propto \text{Tr}(\hat{\rho}_{AB}|i\rangle\langle i| \otimes |j\rangle\langle j|)$.

The description of the TSUP-basis measurement is more involved, because only the superposition of arrivals between certain pairs of time bins can be measured. Recall that the delay introduced in the interferometer's long arm is $\tau_{\text{MZI}} \sim 2.7$ ns and that the measurement arrangement effectively erases the information about which path (long or short) the photon took. Therefore, if there are two time bins $|i\rangle$ and $|j\rangle$ with starting times t_i and $t_j = t_i + \tau_{\text{MZI}}$, respectively, a click in a TSUP detection module in time interval $[t_i, t_i + \Delta t_b]$ is interpreted as a projection onto an equal superposition of photon arrival in time bins $|i\rangle$ and $|j\rangle$. Since the which-path information is deleted using the D/A-basis measurement in the polarization degree of freedom, the information about the phase between time bins $|i\rangle$ and $|j\rangle$ in their superposition is encoded in information about which of the two detectors in the TSUP detection module clicked. The click of a detector in the transmitted path is interpreted as a projection onto $|+_{i,j}\rangle = (1/\sqrt{2})(|i\rangle + |j\rangle)$ and the click of a detector in the reflected path as $|-_{i,j}\rangle = (1/\sqrt{2})(|i\rangle - |j\rangle)$. The basic data unit for the TSUP measurement therefore contains four $d \times d$ matrices M_{TSUP}^{++}, M_{TSUP}^{+-}, M_{TSUP}^{-+}, and M_{TSUP}^{--}, which capture time-of-arrival information as well as which detector [transmitted $(+)$ or reflected $(-)$ path] in Alice's and Bob's TSUP measurement modules clicked. As an example, consider matrix element $m_{i,j}^{+-}$ of M_{TSUP}^{+-}, which contains the number of coincident projections onto $|+_{i,i'}\rangle$ on Alice's side and $|-_{j,j'}\rangle$ on Bob's side, where $t_{i'} = t_i + \tau_{\text{MZI}}$ and $t_{j'} = t_j + \tau_{\text{MZI}}$. Further complication comes from the fact that not all projections captured in four TSUP correlation matrices belong to the chosen time frame and therefore their detection is not a valid measurement outcome for the chosen Hilbert space. As an example, consider the $d-1$st row of an arbitrary TSUP correlation matrix that contains the number of projections onto a superposition between time bin $|d-1\rangle$ and a time bin starting at time $t_{d-1} + \tau_{\text{MZI}}$ in Alice's lab. Such a projection clearly falls outside of the time frame defined by time bins $|0\rangle, \ldots, |d-1\rangle$ with $t_0 < t_1 < \cdots t_{d-1}$. In this

sense the TSUP detection module can project onto an overcomplete set of projectors, some of which even fall outside of the chosen discretization. In order to obtain well-defined and normalized outcome probabilities in the TSUP basis, the set of projectors $\{|+_{i,j}\rangle, |-_{i,j}\rangle\}$, which are contained in the four TSUP correlation matrices, need to contain at least one full basis of the Hilbert space associated to the chosen time frame.

The presented results are obtained by setting the time-frame length to $2\tau_{\text{MZI}} = 5.4$ ns. Each time frame is subsequently divided into time bins of equal size Δt_b. The choice of Δt_b influences the dimensionality d of the Hilbert space as $d = 2\tau_{\text{MZI}}/\Delta t_b$. In our experiment, the highest chosen dimensionality is $d = 36$ ($\Delta t_b = 150$ ps) and the smallest one $d = 4$ ($\Delta t_b = 1350$ ps). Importantly, if even values of d are used in postprocessing, then the four TSUP data matrices contain coincidence counts for projections onto $\{|+_{i,i+d/2}\rangle, |-_{i,i+d/2}\rangle\}$ for each $i \in \{0, \ldots, d/2 - 1\}$. Such a set of vectors forms a complete basis of the chosen d-dimensional Hilbert space and thus defines a normalized projective measurement. Coincidence counts corresponding to these projectors can be straightforwardly normalized into estimates of outcome probabilities, which are subsequently used in the key-rate and entanglement witness calculations.

Having defined the Hilbert spaces and measurements used in the postprocessing, it remains to define additional measurement assumptions. We process the measurement by splitting the data into 200 s intervals and sequence them into time frames. Therefore, both TOA and TSUP matrices used for the calculation of results in different times contain coincident counts from 200 s integration of time frames. In order to deal with nonconclusive measurement rounds, we employ a fair-sampling assumption. In the ideal case, in each of the time frames exactly one detector would click in both Alice's and Bob's labs—we call such events *valid time frames*. Time frames in which neither party or just a single party detects a photon are discarded, while multiclick time frames are assigned random outcomes, which are added to the data matrices produced by valid time frames.

The signal-to-noise ratio in the valid coincidences in the measurements depends very strongly on the environmental conditions (see Table I).

TABLE I. Frame statistics from the best and the least achievable key rate in SUP (time-superposition) basis (see Fig. 3). The valid frame ratio is the ratio of valid frames to all possible frames in the integration time. The signal-to-noise ratio (SNR) is the ratio of valid frames and the coincidence frames which detect a photon in the same bin.

Dimension	Time	Valid frame ratio	Valid frames	SNR (%)
6	03:20	2.49×10^{-6}	91152	58.5
18	05:35	2.35×10^{-6}	86943	19.8

5. Qubit subspace entanglement witness

As pointed out in Ref. [29], strong entanglement robustness can be observed in subspaces of high-dimensional entangled states. Therefore, we evaluate a qubit entanglement witness in 2×2 subspaces of the whole $(d \times d)$-dimensional Hilbert space. Recall that time frames of even dimensionality d are used and therefore both Alice's and Bob's local d-dimensional Hilbert space can be interpreted as a direct sum of $d/2$ qubit Hilbert spaces $\mathcal{H}_2^{(i)}$, where index i runs from 0 to $d/2 - 1$. Further, each subspace $\mathcal{H}_2^{(i)}$ is spanned by computational basis vectors $|i\rangle$ and $|i + d/2\rangle$. In the subspace postselection, only coincidences where both Alice and Bob register a click in the same subspace are kept and to each subspace two measurements are associated. The first measurement is a projection onto the time-of-arrival basis spanned by $\{|i\rangle, |i + d/2\rangle\}$ and the second one is a projection onto $\{|+_{i,i+d/2}\rangle, |-_{i,i+d/2}\rangle\}$. Both of these form a complete set of projectors in their respective qubit subspaces and thus can be renormalized into joint outcome probabilities. Importantly, the employed entanglement witness takes into account only probabilities of matching outcomes in both measurements. In each subspace, the relative frequency of matching outcomes for the TOA measurement is calculated as $p_{\text{TOA}}^i = (m_{i,i} + m_{i+d/2,i+d/2})/(m_{i,i} + m_{i,i+d/2} + m_{i+d/2,i} + m_{i+d/2,i+d/2})$, where $m_{a,b}$ are elements of the raw count matrix M_{TOA} defined in the previous section. Similarly, the relative frequency of matching outcomes for the TSUP measurement is calculated as $p_{\text{TSUP}}^i = (m_{i,i}^{++} + m_{i,i}^{--})/(m_{i,i}^{++} + m_{i,i}^{+-} + m_{i,i}^{-+} + m_{i,i}^{--})$, where all $m_{i,i}^{\pm,\pm}$ are elements of the corresponding matrix $M_{\text{TSUP}}^{\pm\pm}$. The measured state is entangled [49] in subspace $\mathcal{H}_2^{(i)} \times \mathcal{H}_2^{(i)}$ if and only if $p_{\text{TOA}}^i + p_{\text{TSUP}}^i > 3/2$. In Fig. 2, the average value of the witness calculated over all $d/2$ qubit subspaces is plotted. Succinctly, for each subspace i this quantity can be expressed using a witness operator:

$$
\begin{aligned}
\hat{\mathcal{W}}_d^{(i)} = & |i\rangle\langle i| \oplus |i\rangle\langle i| \\
& + |i + d/2\rangle\langle i + d/2| \oplus |i + d/2\rangle\langle i + d/2| \\
& + |+_{i,i+d/2}\rangle\langle +_{i,i+d/2}| \oplus |+_{i,i+d/2}\rangle\langle +_{i,i+d/2}| \\
& + |-_{i,i+d/2}\rangle\langle -_{i,i+d/2}| \oplus |-_{i,i+d/2}\rangle\langle -_{i,i+d/2}|, \quad \text{(A2)}
\end{aligned}
$$

with a condition that $\text{Tr}(\hat{\rho}_{AB}^{(i)} \hat{\mathcal{W}}_d^{(i)}) > 3/2$, where $\hat{\rho}_{AB}^{(i)}$ is the projection of the experimental state $\hat{\rho}_{AB}$ into the ith subspace.

6. Key-rate estimation

For each subspace $\mathcal{H}_2^{(i)} \otimes \mathcal{H}_2^{(i)}$ defined in the previous section, the asymptotic key fraction (i.e., key per subspace coincidence) can be estimated using the Koashi-Preskill [50] formula:

$$
K(i) \geq 1 - H(p_{\text{TOA}}^i) - H(p_{\text{TSUP}}^i), \quad \text{(A3)}
$$

where $H(\cdot)$ is the Shannon entropy function. To obtain the overall average key fraction K, individual key-rate fractions $K(i)$ of all subspaces are averaged. The key rate per second can in turn be calculated by multiplying K by the number of subspace coincidences per second. Increasing the dimension increases the information shared by each transmitted and accepted photon pair [see Fig. 4(a)], but on the other hand lessens the number of photon-pair detection events accepted by the protocol and therefore reduces the key rate [see Fig. 4(b)]. Note that in each integration interval of 200 s for which we estimate the key rate (see Fig. 3), we obtain coincidence counts ranging from 101 000 (during the night) to 28 000 (after dawn).

7. Time synchronization

In our implementation the two communicating labs are separated by 10.2 km. Although the signal travels with the
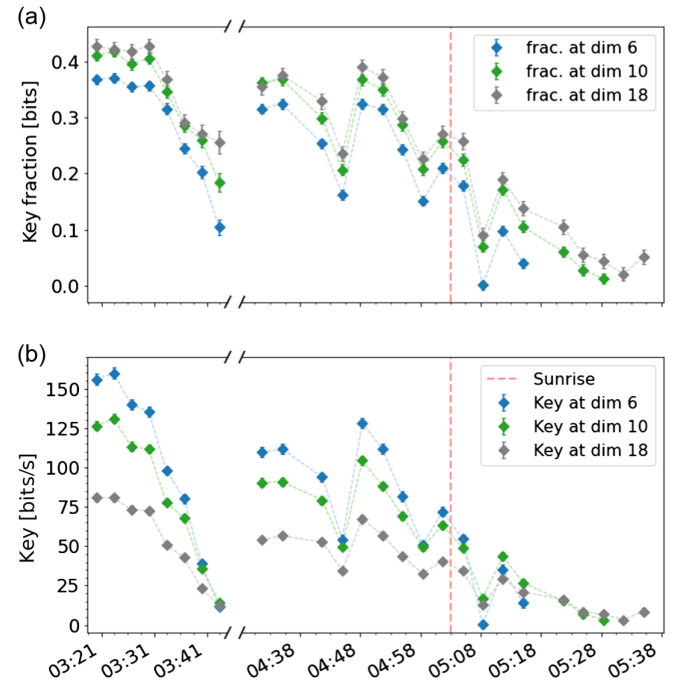

FIG. 4. Key rate versus key fraction. A closer look at achievable asymptotic key rate. (a) Key fraction—the achievable key rate per postselected coincidence—plotted for different values of discretization dimension. To obtain key rate in bits per second, shown in (b), this value is multiplied by the number of subspace coincidences in the given 200 s integration window. Panel (a) shows that discretizations consistently achieve the highest key fraction with the highest local dimension d. However, the highest key fraction does not lead to the overall highest key rate per second in most cases, as using higher-dimensional discretization also leads to a smaller number of subspace coincidences per second. The lines serve as guides for the eye.
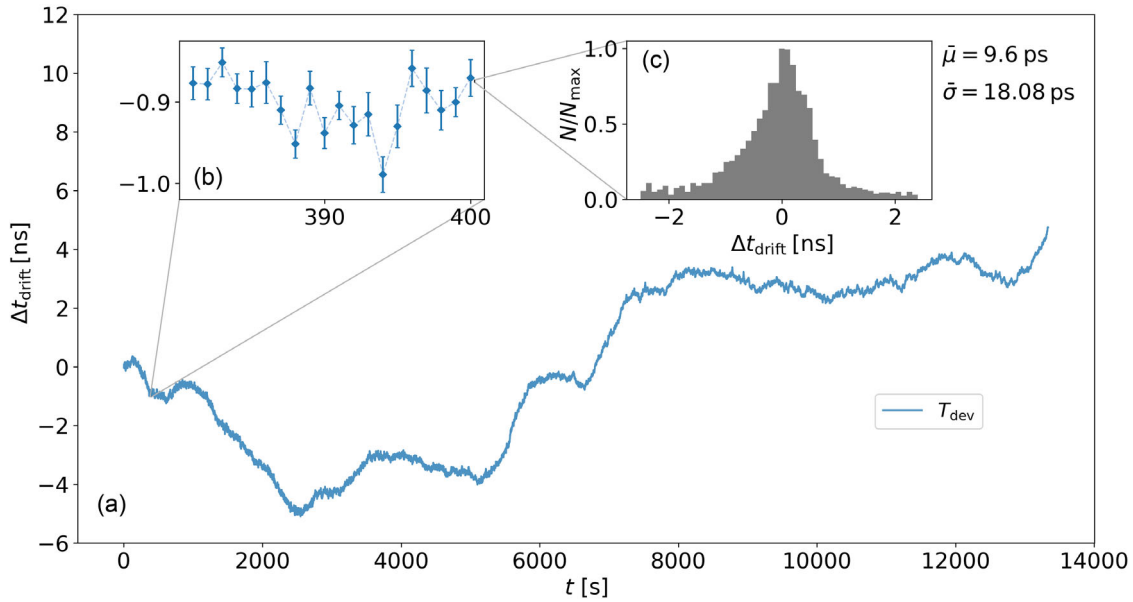
FIG. 5. Clock drift. A closer look at relative clock drift T_{dev}. (a) T_{dev} is displayed over time in seconds from time 04:25 onward. It shows that over a long measurement the relative drift between the Rb clocks is in the order of 10 ns. In panel (b) a 20 s interval gives a better view on the change of T_{dev} per second and the residual timing error. (c) Coincidence peak for the 400th second. The accumulated offset ($\Delta t_{\text{off}} = 812$ ps) of the previous second is already subtracted. That leaves a residual error of $\bar{\mu} = 9.6$ ps to add to the offset.

speed of light there is a significant timing delay introduced between Alice and Bob, concerning the time-frame and time-bin sizes used in the experiment. The delay is additionally increased by electronic jitter and group velocities caused by signal processing. All these effects combine to 33.802 µs and can be subtracted as an offset from Bob's time tags. This operation leaves a timing uncertainty error in the order of 10 ns which is still too large to process the time bins efficiently. The residual error is caused by the relative drift T_{dev} of the two Rb clocks on each end of the experiment. To further improve our timing accuracy we use the intrinsic property of the SPDC to produce time-correlated photon pairs within the coherence time of $\tau_p \sim 3$ ps. After splitting and distributing the correlated photons to each communication partner, we chop the time tag streams into 1 s chunks and perform an intensity correlation function to an offset corrected chunk of Bob with the corresponding chunk of Alice [51]. This results in a photon coincidence distribution with a peak at the expectation value $\bar{\mu}$. The value of $\bar{\mu}$ is calculated every second and added to the offset to track the coincidence peak. This results in a residual synchronization error in the order of $\bar{\sigma} = 20$ ps (see Fig. 5). With higher count rates one can increase the accuracy further. To not diminish the key rate and to increase the timing precision, we use correlations between TOA and TSUP basis of Alice and Bob. These are caused by the 3 dB beam splitters responsible for the passive the basis choice (see Fig. 1), and in any case contribute a 3 db loss to the link budget.

[1] Nicolas Gisin, Grégoire Ribordy, Wolfgang Tittel, and Hugo Zbinden, *Quantum Cryptography*, Rev. Mod. Phys. **74**, 145 (2002).

[2] Feihu Xu, Xiongfeng Ma, Qiang Zhang, Hoi-Kwong Lo, and Jian-Wei Pan, *Secure Quantum Key Distribution with Realistic Devices*, Rev. Mod. Phys. **92**, 025002 (2020).

[3] Ryszard Horodecki, Paweł Horodecki, Michał Horodecki, and Karol Horodecki, *Quantum Entanglement*, Rev. Mod. Phys. **81**, 865 (2009).

[4] Sören Wengerowsky, Siddarth Koduru Joshi, Fabian Steinlechner, Hannes Hübel, and Rupert Ursin, *An Entanglement-Based Wavelength-Multiplexed Quantum Communication Network*, Nature (London) **564**, 225 (2018).

[5] Jeongwan Jin, Sascha Agne, Jean-Philippe Bourgoin, Yanbao Zhang, Norbert Lütkenhaus, and Thomas Jennewein, *Demonstration of Analyzers for Multimode Photonic Time-Bin Qubits*, Phys. Rev. A **97**, 043847 (2018).

[6] Ivan Marcikic, Hugues De Riedmatten, Wolfgang Tittel, Hugo Zbinden, Matthieu Legré, and Nicolas Gisin, *Distribution of Time-Bin Entangled Qubits over 50 km of Optical Fiber*, Phys. Rev. Lett. **93**, 180502 (2004).

[7] T. Honjo, S. W. Nam, H. Takesue, Q. Zhang, H. Kamada, Y. Nishida, O. Tadanaga, M. Asobe, B. Baek, R. Hadfield, S. Miki, M. Fujiwara, M. Sasaki, Z. Wang, K. Inoue, and Y. Yamamoto, *Long-Distance Entanglement-Based Quantum Key Distribution over Optical Fiber*, Opt. Express **16**, 19118 (2008).

[8] Boris Korzh, Charles Ci Wen Lim, Raphael Houlmann, Nicolas Gisin, Ming Jun Li, Daniel Nolan, Bruno

Sanguinetti, Rob Thew, and Hugo Zbinden, *Provably Secure and Practical Quantum Key Distribution over 307 km of Optical Fibre*, Nat. Photonics **9,** 163 (2015).

[9] Hua-Lei Yin, Teng-Yun Chen, Zong-Wen Yu, Hui Liu, Li-Xing You, Yi-Heng Zhou, Si-Jing Chen, Yingqiu Mao, Ming-Qi Huang, Wei-Jun Zhang *et al.*, *Measurement-Device-Independent Quantum Key Distribution over a 404 km Optical Fiber*, Phys. Rev. Lett. **117,** 190501 (2016).

[10] Rupert Ursin, F Tiefenbacher, T Schmitt-Manderbach, H Weier, Thomas Scheidl, M Lindenthal, B Blauensteiner, T Jennewein, J Perdigues, P Trojek *et al.*, *Entanglement-Based Quantum Communication over 144 km*, Nat. Phys. **3,** 481 (2007).

[11] Alessandro Fedrizzi, Rupert Ursin, Thomas Herbst, Matteo Nespoli, Robert Prevedel, Thomas Scheidl, Felix Tiefenbacher, Thomas Jennewein, and Anton Zeilinger, *High-Fidelity Transmission of Entanglement over a High-Loss Free-Space Channel*, Nat. Phys. **5,** 389 (2009).

[12] Jian-Yu Wang, Bin Yang, Sheng-Kai Liao, Liang Zhang, Qi Shen, Xiao-Fang Hu, Jin-Cai Wu, Shi-Ji Yang, Hao Jiang, Yan-Lin Tang *et al.*, *Direct and Full-Scale Experimental Verifications towards Ground–Satellite Quantum Key Distribution*, Nat. Photonics **7,** 387 (2013).

[13] Sebastian Nauerth, Florian Moll, Markus Rau, Christian Fuchs, Joachim Horwath, Stefan Frick, and Harald Weinfurter, *Air-to-Ground Quantum Communication*, Nat. Photonics **7,** 382 (2013).

[14] Fabian Steinlechner, Sebastian Ecker, Matthias Fink, Bo Liu, Jessica Bavaresco, Marcus Huber, Thomas Scheidl, and Rupert Ursin, *Distribution of High-Dimensional Entanglement via an Intra-City Free-Space Link*, Nat. Commun. **8,** 15971 (2017).

[15] Sheng-Kai Liao, Wen-Qi Cai, Wei-Yue Liu, Liang Zhang, Yang Li, Ji-Gang Ren, Juan Yin, Qi Shen, Yuan Cao, Zheng-Ping Li *et al.*, *Satellite-to-Ground Quantum Key Distribution*, Nature (London) **549,** 43 (2017).

[16] Juan Yin, Yuan Cao, Yu-Huai Li, Sheng-Kai Liao, Liang Zhang, Ji-Gang Ren, Wen-Qi Cai, Wei-Yue Liu, Bo Li, Hui Dai *et al.*, *Satellite-Based Entanglement Distribution over 1200 Kilometers*, Science **356,** 1140 (2017).

[17] Hideki Takenaka, Alberto Carrasco-Casado, Mikio Fujiwara, Mitsuo Kitamura, Masahide Sasaki, and Morio Toyoshima, *Satellite-to-Ground Quantum-Limited Communication Using a 50-kg-Class Microsatellite*, Nat. Photonics **11,** 502 (2017).

[18] Sheng-Kai Liao, Jin Lin, Ji-Gang Ren, Wei-Yue Liu, Jia Qiang, Juan Yin, Yang Li, Qi Shen, Liang Zhang, Xue-Feng Liang *et al.*, *Space-to-Ground Quantum Key Distribution Using a Small-Sized Payload on Tiangong-2 Space Lab*, Chin. Phys. Lett. **34,** 090302 (2017).

[19] Juan Yin, Yu-Huai Li, Sheng-Kai Liao, Meng Yang, Yuan Cao, Liang Zhang, Ji-Gang Ren, Wen-Qi Cai, Wei-Yue Liu, Shuang-Lin Li *et al.*, *Entanglement-Based Secure Quantum Cryptography over 1,120 Kilometres*, Nature (London) **582,** 501 (2020).

[20] Paul G. Kwiat, *Hyper-Entangled States*, J. Mod. Opt. **44,** 2173 (1997).

[21] Julio T. Barreiro, Nathan K. Langford, Nicholas A. Peters, and Paul G. Kwiat, *Generation of Hyperentangled Photon Pairs*, Phys. Rev. Lett. **95,** 260501 (2005).

[22] Alexey Tiranov, Sébastien Designolle, Emmanuel Zambrini Cruzeiro, Jonathan Lavoie, Nicolas Brunner, Mikael Afzelius, Marcus Huber, and Nicolas Gisin, *Quantification of Multidimensional Entanglement Stored in a Crystal*, Phys. Rev. A **96,** 040303 (2017).

[23] Anthony Martin, Thiago Guerreiro, Alexey Tiranov, Sébastien Designolle, Florian Fröwis, Nicolas Brunner, Marcus Huber, and Nicolas Gisin, *Quantifying Photonic High-Dimensional Entanglement*, Phys. Rev. Lett. **118,** 110501 (2017).

[24] A. Cuevas, G. Carvacho, G. Saavedra, J. Cariñe, W. A. T. Nogueira, M. Figueroa, Adan Cabello, P. Mataloni, G. Lima, and G. B. Xavier, *Long-Distance Distribution of Genuine Energy-Time Entanglement*, Nat. Commun. **4,** 2871 (2013).

[25] H. Bechmann-Pasquinucci and W. Tittel, *Quantum Cryptography Using Larger Alphabets*, Phys. Rev. A **61,** 062308 (2000).

[26] Daniele Cozzolino, Beatrice Da Lio, Davide Bacco, and Leif Katsuo Oxenløwe, *High-Dimensional Quantum Communication: Benefits, Progress, and Future Challenges*, Adv. Quantum Technol. **2,** 1900038 (2019).

[27] Tian Zhong, Hongchao Zhou, Robert D. Horansky, Catherine Lee, Varun B. Verma, Adriana E. Lita, Alessandro Restelli, Joshua C. Bienfang, Richard P. Mirin, Thomas Gerrits *et al.*, *Photon-Efficient Quantum Key Distribution Using Time–Energy Entanglement with High-Dimensional Encoding*, New J. Phys. **17,** 022002 (2015).

[28] Irfan Ali-Khan, Curtis J. Broadbent, and John C. Howell, *Large-Alphabet Quantum Key Distribution Using Energy-Time Entangled Bipartite States*, Phys. Rev. Lett. **98,** 060503 (2007).

[29] Sebastian Ecker, Frédéric Bouchard, Lukas Bulla, Florian Brandt, Oskar Kohout, Fabian Steinlechner, Robert Fickler, Mehul Malik, Yelena Guryanova, Rupert Ursin *et al.*, *Overcoming Noise in Entanglement Distribution*, Phys. Rev. X **9,** 041042 (2019).

[30] Isaac Nape, Valeria Rodríguez-Fajardo, Feng Zhu, Hsiao-Chih Huang, Jonathan Leach, and Andrew Forbes, *Measuring Dimensionality and Purity of High-Dimensional Entangled States*, Nat. Commun. **12,** 1 (2021).

[31] Mirdit Doda, Marcus Huber, Gláucia Murta, Matej Pivoluska, Martin Plesch, and Chrysoula Vlachou, *Quantum Key Distribution Overcoming Extreme Noise: Simultaneous Subspace Coding Using High-Dimensional Entanglement*, Phys. Rev. Appl. **15,** 034003 (2021).

[32] Xiao-Min Hu, Chao Zhang, Yu Guo, Fang-Xiang Wang, Wen-Bo Xing, Cen-Xiao Huang, Bi-Heng Liu, Yun-Feng Huang, Chuan-Feng Li, Guang-Can Guo, Xiaoqin Gao, Matej Pivoluska, and Marcus Huber, *Pathways for Entanglement-Based Quantum Communication in the Face of High Noise*, Phys. Rev. Lett. **127,** 110505 (2021).

[33] James D. Franson, *Bell Inequality for Position and Time*, Phys. Rev. Lett. **62,** 2205 (1989).

[34] Mark T. Gruneisen, Mark L. Eickhoff, Scott C. Newey, Kurt E. Stoltenberg, Jeffery F. Morris, Michael Bareian, Mark A. Harris, Denis W. Oesch, Michael D. Oliker, Michael B. Flanagan, Brian T. Kay, Johnathan D. Schiller, and R. Nicholas Lanning, *Adaptive-Optics-Enabled Quantum*

Communication: A Technique for Daytime Space-to-Earth Links, Phys. Rev. Appl. **16,** 014067 (2021).

[35] Taehyun Kim, Marco Fiorentino, and Franco N. C. Wong, *Phase-Stable Source of Polarization-Entangled Photons Using a Polarization Sagnac Interferometer*, Phys. Rev. A **73,** 012316 (2006).

[36] Alessandro Fedrizzi, Thomas Herbst, Andreas Poppe, Thomas Jennewein, and Anton Zeilinger, *A Wavelength-Tunable Fiber-Coupled Source of Narrowband Entangled Photons*, Opt. Express **15,** 15377 (2007).

[37] Jeongwan Jin, Jean-Philippe Bourgoin, Ramy Tannous, Sascha Agne, Christopher J. Pugh, Katanya B. Kuntz, Brendon L. Higgins, and Thomas Jennewein, *Genuine Time-Bin-Encoded Quantum Key Distribution over a Turbulent Depolarizing Free-Space Channel*, Opt. Express **27,** 37214 (2019).

[38] J. E. Debs, N. P. Robins, A. Lance, M. B. Kruger, and J. D. Close, *Piezo-Locking a Diode Laser with Saturated Absorption Spectroscopy*, Appl. Opt. **47,** 5163 (2008).

[39] Caleb Ho, Antía Lamas-Linares, and Christian Kurtsiefer, *Clock Synchronization by Remote Detection of Correlated Photon Pairs*, New J. Phys. **11,** 045011 (2009).

[40] Christopher Spiess, Sebastian Töpfer, Sakshi Sharma, Meritxell Cabrejo Ponce, Daniel Rieländer, and Fabian Steinlechner, *Clock Synchronization with Correlated Photons*, arXiv:2108.13466.

[41] Christoph Spengler, Marcus Huber, Stephen Brierley, Theodor Adaktylos, and Beatrix C. Hiesmayr, *Entanglement Detection via Mutually Unbiased Bases*, Phys. Rev. A **86,** 022311 (2012).

[42] Sebastian Philipp Neumann, Siddarth Koduru Joshi, Matthias Fink, Thomas Scheidl, Roland Blach, Carsten Scharlemann, Sameh Abouagaga, Daanish Bambery, Erik Kerstel, Mathieu Barthelemy *et al.*, Q^3 *Sat: Quantum Communications Uplink to a 3U CubeSat—Feasibility & Design*, Eur. Phys. J. Quantum Technol. **5,** 1 (2018).

[43] Kevin Günthner, Imran Khan, Dominique Elser, Birgit Stiller, Ömer Bayraktar, Christian R. Müller, Karen Saucke, Daniel Tröndle, Frank Heine, Stefan Seel *et al.*, *Quantum-Limited Measurements of Optical Signals from a Geostationary Satellite*, Optica **4,** 611 (2017).

[44] Sheng-Kai Liao, Hai-Lin Yong, Chang Liu, Guo-Liang Shentu, Dong-Dong Li, Jin Lin, Hui Dai, Shuang-Qiang Zhao, Bo Li, Jian-Yu Guan *et al.*, *Long-Distance Free-Space Quantum Key Distribution in Daylight towards Inter-Satellite Communication*, Nat. Photonics **11,** 509 (2017).

[45] S. Bäuml, A. Winter, and D. Yang, *Every Entangled State Provides an Advantage in Classical Communication*, J. Math. Phys. (N.Y.) **60,** 072201 (2019).

[46] Sebastian Ecker, Philipp Sohr, Lukas Bulla, Marcus Huber, Martin Bohmann, and Rupert Ursin, *Experimental Single-Copy Entanglement Distillation*, Phys. Rev. Lett. **127,** 040506 (2021).

[47] Daryl W. Preston, *Doppler-Free Saturated Absorption: Laser Spectroscopy*, Am. J. Phys. **64,** 1432 (1996).

[48] Giuseppe Vallone, Daniele Dequal, Marco Tomasin, Francesco Vedovato, Matteo Schiavon, Vincenza Luceri, Giuseppe Bianco, and Paolo Villoresi, *Interference at the Single Photon Level Along Satellite-Ground Channels*, Phys. Rev. Lett. **116,** 253601 (2016).

[49] Marcus Huber and Julio I. De Vicente, *Structure of Multidimensional Entanglement in Multipartite Systems*, Phys. Rev. Lett. **110,** 030501 (2013).

[50] Masato Koashi and John Preskill, *Secure Quantum Key Distribution with an Uncharacterized Source*, Phys. Rev. Lett. **90,** 057902 (2003).

[51] Jianwei Lee, Lijiong Shen, Adrian Nugraha Utama, and Christian Kurtsiefer, *Absolute Clock Synchronization with a Single Time-Correlated Photon Pair Source over a 10 km Optical Fibre*, Opt. Express **30,** 18530 (2022).